JOM, Vol. 75, No. 7, 2023
https://doi.org/10.1007/s11837-023-05866-8

Computational Design of Bio-inspired Mechanical Metamaterials Based on Lipidic Cubic Phases

ZILONG ZHAO,[1] YUNYA LIU,[1] and PAI WANG [1,2]

1.—Department of Mechanical Engineering, University of Utah, Salt Lake City, UT 84112, USA.
2.—e-mail: pai.wang@utah.edu

We report a family of designs and numerical simulations of cubic elastic metamaterials inspired by lipidic cubic phases (LCPs). Since LCPs are triply periodic minimal surfaces spontaneously formed in natural physical and chemical processes, our designs can be suitable candidates for high-throughput fabrication through self-assembly. This potential advantage may overcome the challenge of time cost in the traditional unit-by-unit additive manufacturing processes. We analyze the bio-inspired designs of primitive, gyroid, and diamond configurations by focusing on their geometry, symmetry, and elastic behaviors. We lay out the detailed numerical simulation procedures to extract the effective macroscopic elastic moduli of cubic metamaterials. We proceed with parametric studies regarding internal surface thickness and constituent base material properties. We also discuss their implications in terms of the metamaterials' isotropy and compressibility. Our results can provide guidelines for next-generation elastic metamaterials that can be massively produced with high efficiency.

INTRODUCTION

Metamaterials are architected composites whose properties and functionalities derive mainly from their internal geometries. They have found numerous applications in acoustics,[1–4] photonics,[5–9] fluid dynamics,[10–12] thermodynamics,[13] and biomedical devices.[14,15] Most metamaterials to date are fabricated in additive manufacturing processes such as popular 3D printing techniques.[3,16–20] The time cost of fabrication could become a serious bottleneck in the future development of this research field, especially when we need a sample of millions of unit cells.[21–23] It is a long-standing challenge to search for high-throughput alternatives as more efficient approaches in design and fabrication.

In the realm of biophysics and biochemistry, self-assembly is an efficient way to form many different geometrical patterns.[24] In particular, the lipid bilayer, abundant in most cell membranes, can self-organize into crystalline morphological phases with spatial periodicity.[25] While lamellar and hexagonal phases[26] are periodic in one and two dimensions, "lipidic cubic phases" (LCPs)[27] are periodic in all three dimensions. These novel structures can facilitate protein crystallization,[28] gene therapy,[29] medical imaging,[30] and medical device development.[31–34] Although most research on LCPs focused on the biophysical behaviors[35–42] and biochemical functionalities,[43–48] their geometrical/rheological properties are an important aspect as well.[49–54] For example, LCP phases have been proven to be the most rigid crystallized phases[55] compared to other morphologies.[56–61]

Lipid molecules are hydrophilic at one end and hydrophobic at the other end. They can spontaneously morph into LCPs in aqueous solutions because of the strong effects of surface tension, which locally minimizes the surface area and results in zero mean curvature everywhere.[62] The building blocks here assemble into cubic unit cells, which in turn self-tessellate into nicely periodic and intersection-free arrangements in three dimensions, known as triply periodic minimal surfaces (TPMS). Using similar mechanisms driven by surface tension, La et al.[38] reported the self-assembly of amphiphilic dendritic-linear block copolymers into polymer cubosomes, while Jain et al.[63] discovered

(Received February 2, 2023; accepted April 19, 2023; published online May 30, 2023)

that poly diblock copolymers can form various ordered and disordered phases through self-assembly. Additionally, Percec et al.[64] observed the self-assembly of Janus dendrimers, resulting in dendrimersomes with diverse structures. Hence, we expect that similar processes exploiting nature's tendency to minimize surface energy could be developed as potential high-throughput techniques to manufacture next-generation cubic metamaterials.

Previous research efforts on TPMS include solid[65] and sheet-like networks.[66,67] Furthermore, other researchers also investigated different geometries within the TPMS families.[68–72] In addition, studies also reported the effective behaviors of TPMS architecture with different base materials, including ceramics,[73] stainless steel,[74] metals,[75] and polymers.[69,76,77] However, most studies focus on one or two loading directions only for the uni-axial deformation behavior. Building on the existing literature, we draw the attention to multi-directional properties of the TPMS structures with detailed analyses of the anisotropic metamaterial behaviors in full.

In this article, we employ bio-mimicry to design cubic elastic metamaterials based on LCP morphologies. We investigate the anisotropic behaviors of primitive, gyroid, and diamond structures in terms of direction-dependent effective elastic properties. First, we establish a rigorous framework to construct the metamaterial geometries, perform numerical simulations, and extract the effective properties. Then, we conduct parametric studies on the surface thickness and base material properties. Lastly, we further analyze our results in terms of effective anisotropy and effective compressibility. Our findings can provide guidance for the design, fabrication, and characterization of an assortment of cubic elastic metamaterials for load-bearing purposes.

GEOMETRY, SYMMETRY, AND ELASTICITY

Bio-inspired Pattern Designs

Depending on the temperature and solvent composition,[27] three different types of LCPs may form: primitive (P), gyroid (G), and diamond (D). All are triply periodic minimal surfaces (TPMS) and can be mathematically defined as the following surfaces in the three-dimensional Primitive (P): Cartesian space.[78,79]

Primitive (P):

$$\cos X + \cos Y + \cos Z = 0, \tag{1a}$$

Gyroid (G):

$$\sin X \cos Y + \sin Y \cos Z + \cos X \sin Z = 0, \tag{1b}$$

Diamond (D):

$$\sin X \sin Y \sin Z + \sin X \cos Y \cos Z + \cos X \sin Y \cos Z + \cos X \cos Y \sin Z = 0. \tag{1c}$$

In these equations, $X = 2\alpha\pi x, Y = 2\beta\pi y, Z = 2\gamma\pi z$, where x, y and z are the spatial coordinates, and α, β, and γ are parameters that control the size of the unit cell in three different Cartesian directions, respectively. Hence, the unit cell volume is inversely proportional to the product of all three control parameters, $\alpha\beta\gamma$. Figure 1 shows our computational rendering of the geometries constructed using Eq. 1a–c for primitive, gyroid, and diamond TPMS, respectively. Both unit cells (left column) and the $3 \times 3 \times 3$ assemblies (right column) are illustrated.

Spatial Symmetries

On one hand, all three geometries in Fig. 1 belong to the same O_h ("O" for all symmetries of a regular octahedron, "h" for the mirror symmetry about the

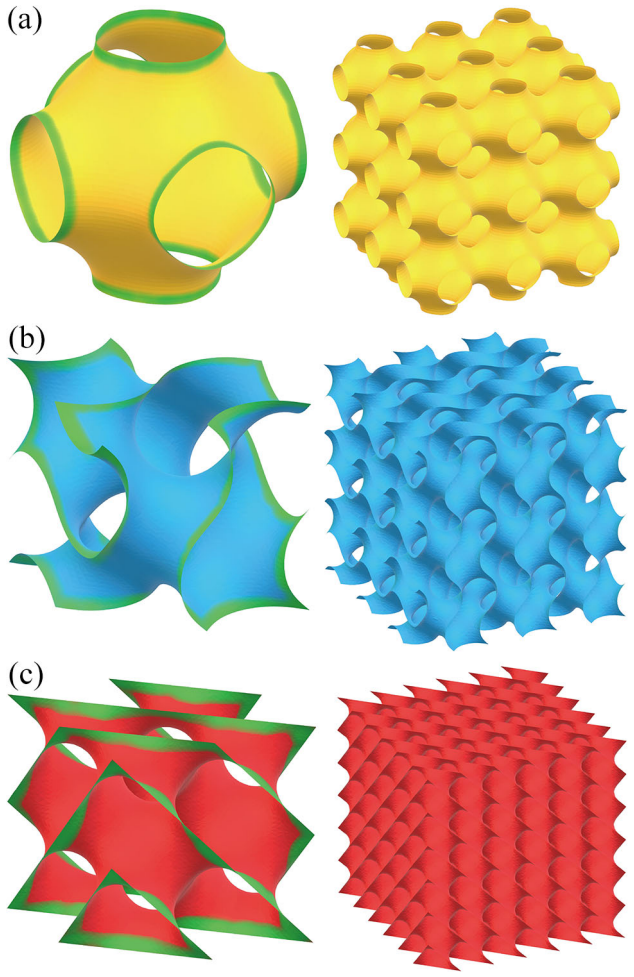

Fig. 1. Triply periodic minimal surfaces (TPMS) based on lipidic cubic phase (LCP) morphologies: (a) primitive, (b) gyroid, (c) diamond. Left column: unit cells; right column: $3 \times 3 \times 3$ assemblies.

horizontal plane) crystallographic point group with 48 elements of symmetry in the following types: inversion, mirror plane, and two-, three-, and four-fold rotational symmetries. Here, "n-fold" means rotational symmetry operations of $(360/n)^\circ$. On the other hand, we have three different types of crystallographic space groups:

- $Im\bar{3}m$ for primitive;
- $Ia\bar{3}d$ for gyroid;
- $Pn\bar{3}m$ for diamond.

A total of four indices completely describe the symmetries in these space groups. The first index represents the type of Bravais lattice in three dimensions ("P" for primitive, "I" for body-centered). The second index represents the translation direction perpendicular to and after (100) plane symmetry operation ("m" for the simple mirror reflection without any glide or translation, "a" for gliding half of the unit cell along one of the lattice vectors, and "n" for gliding half of the unit cell along the diagonal of the mirror plane). The third index, "$\bar{3}$," shows the three-fold rotational symmetry in [111] direction with additional inversion. The fourth index denotes the translation perpendicular to and after (110) plane symmetry operation ("m" for the simple mirror reflection without any glide or translation, "d" for gliding a quarter of the unit cell along the diagonal of the mirror plane).

Cubic Elasticity

The spatial symmetries discussed above guarantee the following form of effective homogenized constitutive relations[80–83] in the linear elastic regime for all three geometries illustrated in Fig. 1.

$$\begin{bmatrix}\sigma_{11}\\ \sigma_{22}\\ \sigma_{33}\\ \sigma_{23}\\ \sigma_{13}\\ \sigma_{12}\end{bmatrix} = \begin{bmatrix}C_{11} & C_{12} & C_{12} & 0 & 0 & 0\\ C_{12} & C_{11} & C_{12} & 0 & 0 & 0\\ C_{12} & C_{12} & C_{11} & 0 & 0 & 0\\ 0 & 0 & 0 & C_{44} & 0 & 0\\ 0 & 0 & 0 & 0 & C_{44} & 0\\ 0 & 0 & 0 & 0 & 0 & C_{44}\end{bmatrix} \begin{bmatrix}\varepsilon_{11}\\ \varepsilon_{22}\\ \varepsilon_{33}\\ \varepsilon_{23}\\ \varepsilon_{13}\\ \varepsilon_{12}\end{bmatrix} \tag{2}$$

where σ_{ij} and ε_{ij} are the components of stress and strain tensors, respectively. This entails that there are only three independent effective moduli: C_{11}, C_{12}, and C_{44}. While isotropic elasticity can be completely specified by two independent parameters, we can designate cubic elasticity as the "simplest" anisotropic elastic behavior since all other types of anisotropic elasticity would need more than three independent material parameters. It is also important to emphasize that having three-fold (120°) rotational symmetries about four axes along the four cubic body diagonals (i.e., the space diagonals) is sufficient to guarantee the cubic elasticity detailed by Eq. 2. Contrary to some popular misconceptions,[84–98] it is not necessary for the unit cell geometry to have any mirror plane or any four-fold (90°) rotational symmetries.[83,99,100]

III. NUMERICAL IMPLEMENTATION

We integrate multiple commercial software platforms to realize the construction, simulation, and post-processing of our numerical analyses.

Geometry Construction

Based on LCP geometry described in Eq. 1a–c, we first create metamaterial unit cell geometries with a discrete set of nodal coordinates in MATLAB. These nodes are used to generate triangular surface elements in the engineering design software SOLIDWORKS where surface meshing is generated via the MESH WIZARD module. Then, we use the mesh to create simulations with element type S3 on the Abaqus finite element platform.

Simulation Setup

We adopt an efficient method to extract effective properties of periodic metamaterials by using only one unit cell in finite element simulations.[101,102] This requires that we apply the appropriate boundary conditions to imitate the internal deformation field in a piece of triply periodic metamaterial with a large number of unit cells. The approach allows us to delineate the intrinsic effective properties of the metamaterials without any influence of external factors.

Aiming at the extraction of effective elastic moduli, C_{11}, C_{12}, and C_{44}, of the metamaterial, we prescribe the macroscopic strain field to each type of unit cell and obtain the corresponding stresses by finite element simulations. In principle, this process can be done in a coordinate-independent manner. For simplicity, we fix the center of the unit cell at the origin of the Cartesian coordinates in our setup. This allows us to prescribe all three displacement components, u_1, u_2, and u_3, for all nodes on the six boundary faces of the cubic unit cell as

$$\begin{bmatrix}u_1\\ u_2\\ u_3\end{bmatrix} = \begin{bmatrix}\varepsilon_{11} & \varepsilon_{12} & \varepsilon_{13}\\ \varepsilon_{12} & \varepsilon_{22} & \varepsilon_{23}\\ \varepsilon_{13} & \varepsilon_{23} & \varepsilon_{33}\end{bmatrix} \begin{bmatrix}X_1\\ X_2\\ X_3\end{bmatrix} \tag{3}$$

where X_1, X_2, and X_3 are the position coordinates of each node on the six boundary faces in the undeformed original configuration. We note that this results in equal and opposite displacements applied to the pair of nodes on the opposing boundary faces.

As shown in Eq. 2, the cubic symmetry guarantees that there is no coupling between normal/shear strains to shear/normal stresses. This fact ensures that we only need to apply two scenarios of strain fields in order to extract all effective metamaterial properties: one uni-axial normal strain (e.g., ε_{11}; see

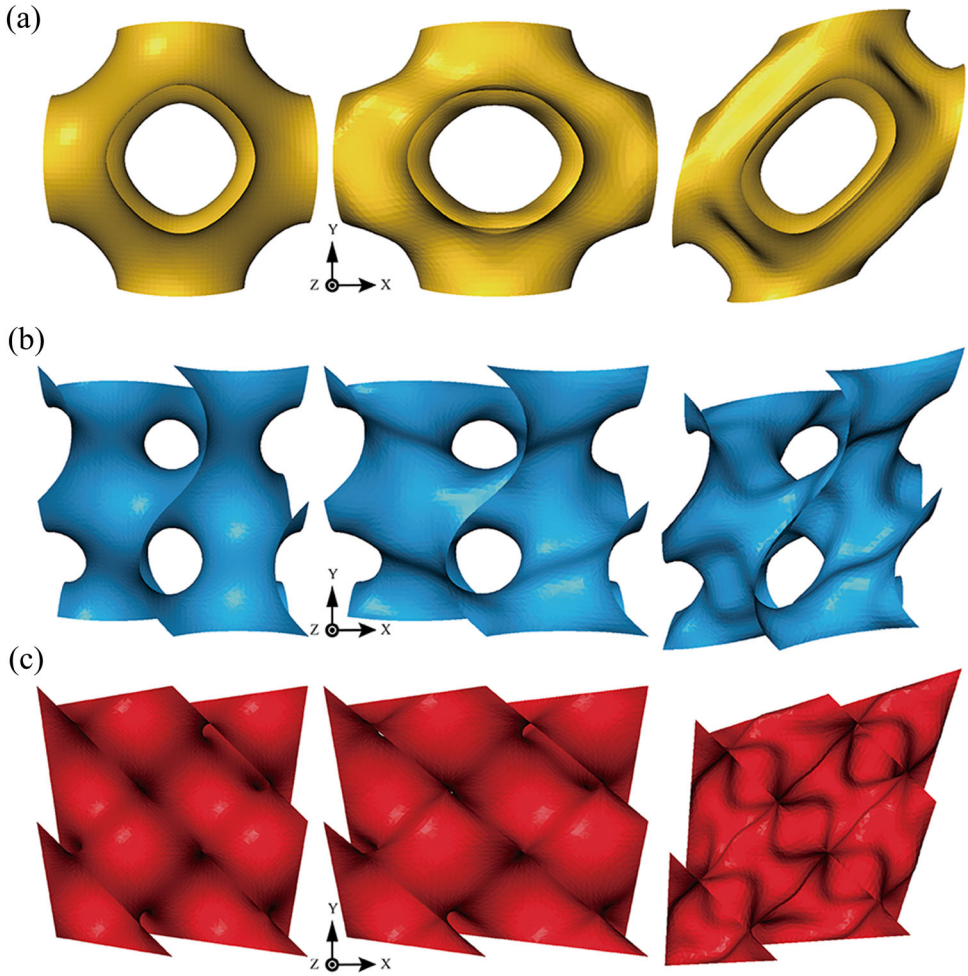

Fig. 2. Original and deformed shapes of metamaterial unit cells: (a) primitive, (b) gyroid, and (c) diamond. The first column shows the undeformed geometries. The second column shows the unit cell shapes after applying normal strain in the horizontal direction. The third column shows the unit cell shapes after applying shear strain in the plane.

the second column of Fig. 2) and one shear strain (e.g., ε_{12}; see the third column of Fig. 2). Since there is no normal shear coupling in the linear regime, we can combine them and prescribe the following strain tensor in all simulations:

$$\boldsymbol{\varepsilon}_{\text{input}} = \begin{bmatrix} \varepsilon_{11} & \varepsilon_{12} & 0 \\ \varepsilon_{21} & 0 & 0 \\ 0 & 0 & 0 \end{bmatrix} \tag{4}$$

In all simulations, we use the same constituent base material with isotropic elasticity defined by two parameters, Young's modulus E_0 and Poisson's ratio v_0. Since all effective moduli of the metamaterial design proportionally scale with E_0, we only need to conduct parametric studies on Poisson's ratio of the base constituent material. In addition, we also vary the thickness, t, of the TPMS geometry in each unit cell in the range from $t/a = 0.001$ to $t/a = 0.1$ where a denotes the length of the cubic unit cell or, equivalently, the lattice constant of the metamaterial.

Post-Simulation Data Extraction

To calculate the homogenized effective stress components, we use the same sets of nodes where we prescribe the displacement boundary conditions. We extract the reaction force vector, F_i for $i = 1, 2, 3$, at each of those nodes and further calculate the numerical values of the stress components by

$$\sigma_{ij} = \frac{1}{A_j} \sum F_i. \tag{5}$$

where the summation is taken over all nodes on one of the six cubic unit cell boundary surfaces and A_j denotes the surface area. Based on the extracted effective stress tensor, we then calculate the normalized effective moduli of the metamaterial designs

$$C_{11} = (\sigma_{11}/\varepsilon_{11})/E_0, \tag{6a}$$

$$C_{12} = (\sigma_{22}/\varepsilon_{11})/E_0, \tag{6b}$$

$$C_{44} = (\sigma_{12}/\varepsilon_{12})/E_0. \quad (6c)$$

Computational Convergence

To ensure the precision of our numerical results, we conduct mesh convergence studies on each of the metamaterial designs. We vary the number of nodes from $N = 2,000$ to $N = 80,000$ for each unit cell geometry and compare the final results in terms of normalized effective moduli C_{11}, C_{12}, and C_{44}. We calculate comparative percentage differences among cases with different N. The differences become $< 0.1\%$ for $N > 10,000$ in the primitive design, $N > 12,000$ in the gyroid design, and $N > 14,000$ in the diamond design. Thus, we use $N = 10,000$, $N = 12,000$, and $N = 14,000$ for primitive, gyroid, and diamond geometries, respectively, in all plots of results presented in this article.

RESULTS AND DISCUSSION

The LCPs formed in typical biochemical laboratory settings have an average surface thickness ratio of 4% in terms of lipid bilayer thickness over unit cell size.[103] Besides, the lipid bilayers, as a soft bio-material, are usually regarded as nearly incompressible with an average Poisson's ratio of 0.49.[104] Hence, we start with two sets of parametric study: varying Poisson's ratios with a fixed thickness $t/a = 0.04$ of the internal surface and varying thickness with a fixed Poisson's ratio $\nu_0 = 0.49$ of the base constituent material. The results are shown in Fig. 3. Analyzing the data, we first confirm that all cases satisfy the structural stability requirements:[99]

$$C_{11} > 0, \ -C_{11}/2 < C_{12} < C_{11}, \ C_{44} > 0. \quad (7)$$

As shown in Fig. 3 (left column), for the fixed internal surface thickness $t/a = 0.04$, the normalized effective metamaterial moduli, C_{11} and C_{12}, rise monotonically with increasing Poisson's ratio, ν_0, of the base constituent material. In contrast, C_{44} decreases monotonically with increasing Poisson's ratio of the base constituent material. These trends are true for all three unit cell designs. As for Fig. 3 (right column), where Poisson's ratio of the base constituent material is fixed at $\nu_0 = 0.49$, the increase of internal surface thickness, t, makes all normalized effective metamaterial moduli of all three metamaterial designs higher. The elastic stiffness of metamaterials scales almost linearly with the internal surface thickness. A comparison among Fig. 3b, d, and f shows that the diamond design is the stiffest among the three, while the primitive design is the least stiff with equal surface thickness and same constituent material.

Next, we also calculate the effective "principal elasticities" as more informative property parameters of the metamaterials:[80]

$$\kappa = (C_{11} + 2C_{12})/3, \quad (8a)$$

$$\mu_1 = (C_{11} - C_{12})/2, \quad (8b)$$

$$\mu_2 = C_{44}. \quad (8c)$$

where κ denotes the effective bulk modulus, and μ_1, μ_2 denote two direction-dependent effective shear moduli. As eigenvalues of the stiffness matrix in Eq. 2 with different multiplicities, κ, μ_1, and μ_2 are associated with one-, two-, and three-dimensional eigenvector spaces, respectively, in the six-dimensional vector space of all possible elastic strains. Therefore, the structural stability requirements listed in Eq. 7 are exactly equivalent to

$$\kappa > 0, \quad \mu_1 > 0, \quad \mu_2 > 0. \quad (9)$$

Figure 4 presents the parametric results in terms of these normalized effective moduli (i.e., principal stiffness measures) for all three metamaterial designs. They all satisfy Eq. 9. In Fig. 4 (left column), similar trends are present for primitive, gyroid, and diamond designs. For the same fixed internal surface thickness $t = 0.04a$, the normalized effective bulk modulus κ of metamaterials gradually rises with increasing Poisson's ratio of the base constituent material. Unlike κ, the two normalized effective shear moduli μ_1 and μ_2 decrease monotonically. The maximum value of μ_2 is similar for all three unit cell designs at about 0.045 when the base constituent material Poisson's ratio is at $\nu_0 = 0$. We also observe a critical base constituent material Poisson's ratio, ν_c, where the normalized effective bulk modulus κ rises above μ_2 (i.e., we get $\nu_c = \nu_0$ when $\kappa = \mu_2$). For the three different unit cell designs, we have this critical value in the order of $\nu_c(\text{Primitive}) > \nu_c(\text{Gyroid}) > \nu_c(\text{Diamond})$. Compared to primitive and gyroid, κ and μ_2 are consistently higher in diamond design, which has $\kappa \approx \mu_1$ at $\nu_0 = 0$ and $\kappa = \mu_2$ at $\nu_0 = 0.2$.

Figure 4 (right column) plots the normalized effective bulk and shear moduli, κ, μ_1, and μ_2, for all three metamaterial designs with the fixed base constituent material property of $\nu_0 = 0.49$. Similar to data in Fig. 3 (right column), all effectively increase monotonically with increasing internal surface thickness t. Almost all scale linearly with t with the only exception being μ_2 of the primitive design. Among all designs, the diamond configuration has the largest effective bulk modulus κ for all ranges of thickness. The same is true for shear modulus μ_1 and μ_2.

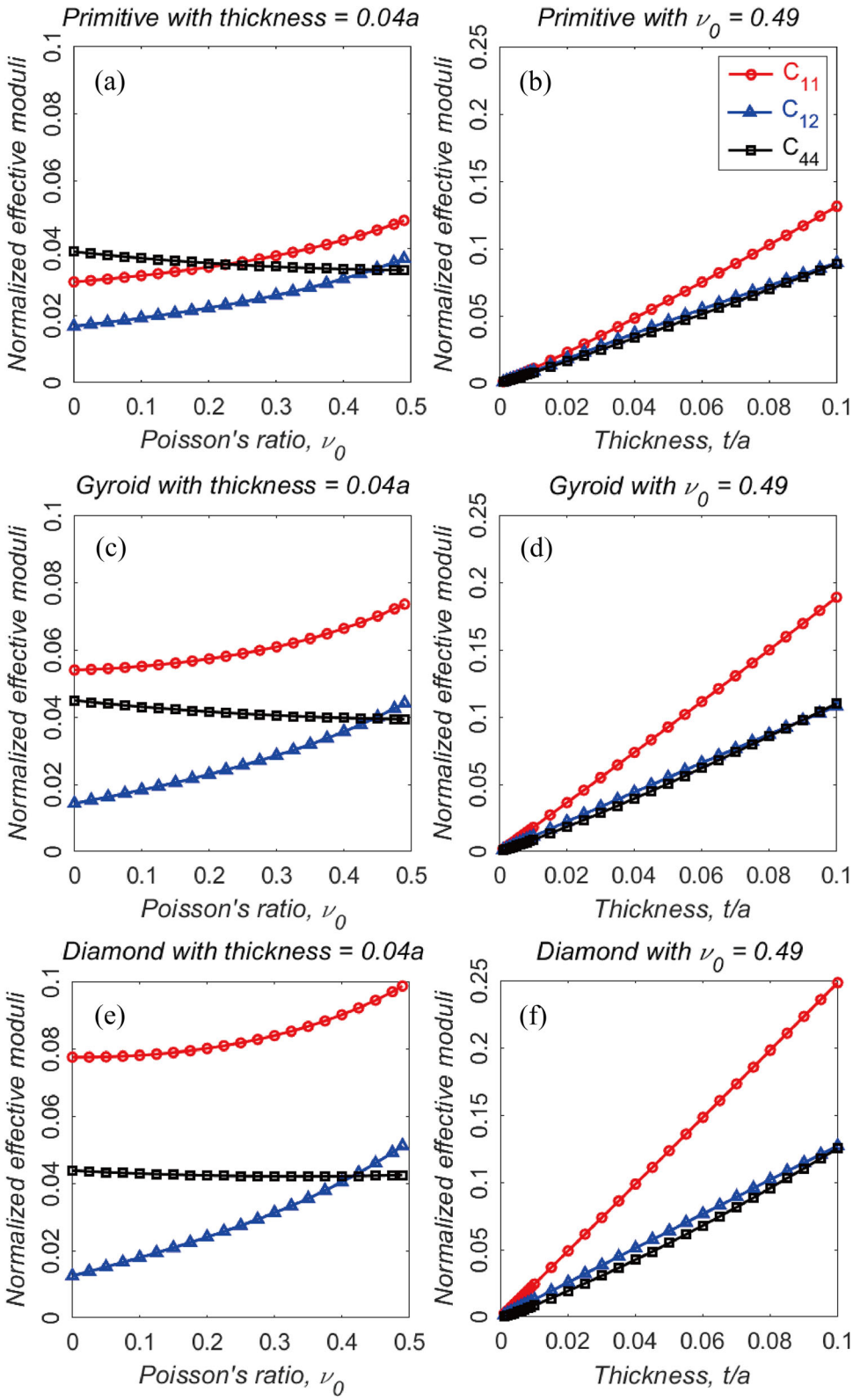

Fig. 3. Effective macroscopic moduli C_{11}, C_{12}, C_{44} of different metamaterial designs with: (a) primitive design with varying Possion's ratios ν_0 at the fixed internal surface thickness $t/a = 0.04$. (b) Primitive design with varying internal surface thicknesses t/a at fixed Possion's ratio $\nu_0 = 0.49$. (c) Gyroid design with varying Possion's ratios ν_0 at the fixed internal surface thickness $t/a = 0.04$. (d) Gyroid design with varying internal surface thicknesses t/a at the fixed Possion's ratio $\nu_0 = 0.49$. (e) Diamond design with varying Possion's ratios ν_0 at the fixed internal surface thickness $t/a = 0.04$. (f) Diamond design with varying internal surface thicknesses t/a at the fixed Possion's ratio $\nu_0 = 0.49$.

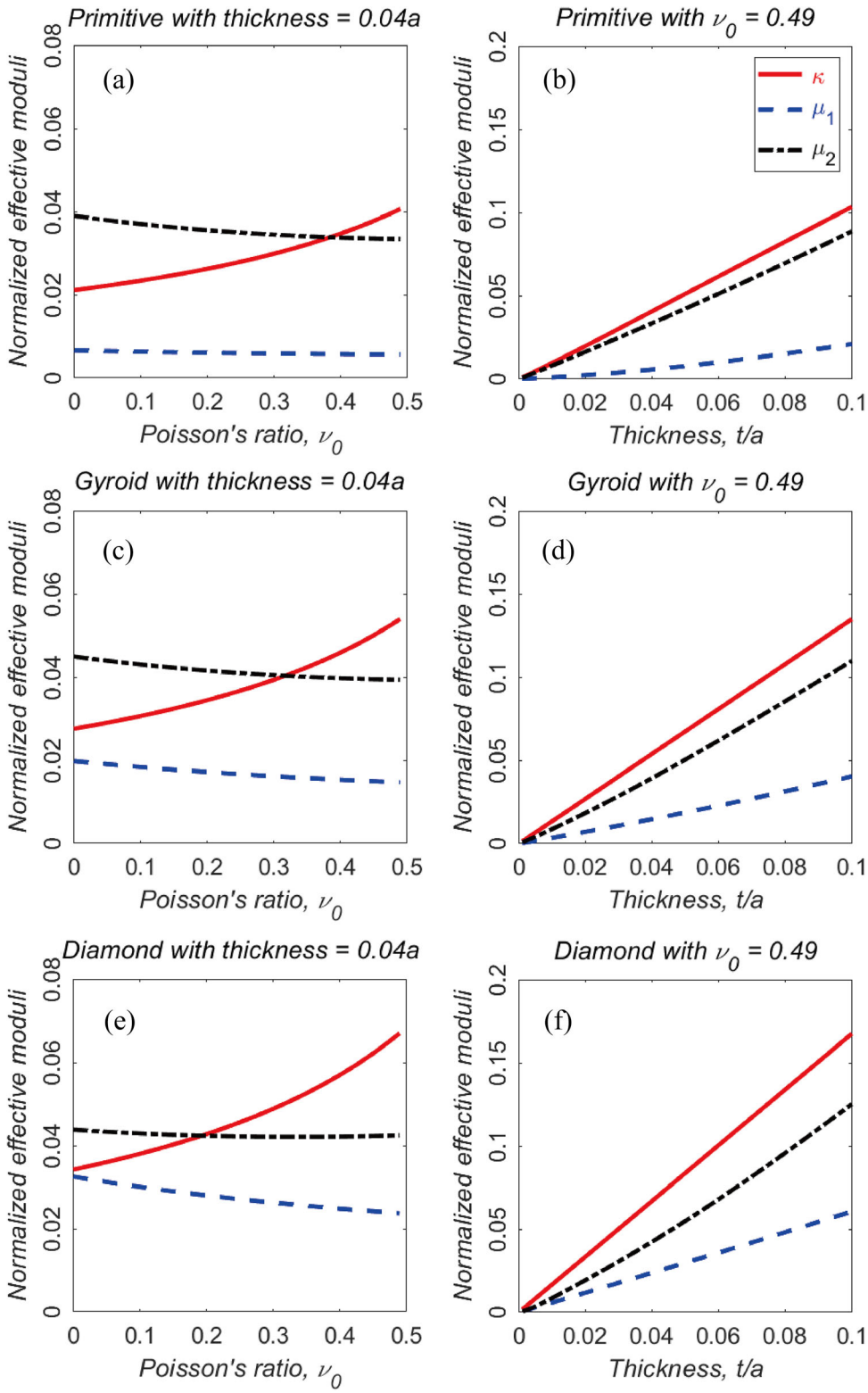

Fig. 4. Effective macroscopic bulk and shear moduli κ, μ_1, μ_2 of different metamaterial designs with: (a) psrimitive design with varying Possion's ratios ν_0 at the fixed internal surface thickness $t/a = 0.04$. (b) Primitive design with varying internal surface thicknesses t/a at the fixed Possion's ratio $\nu_0 = 0.49$. (c) Gyroid design with varying Possion's ratios ν_0 at the fixed internal surface thickness $t/a = 0.04$. (d) Gyroid design with varying internal surface thicknesses t/a at the fixed Possion's ratio $\nu_0 = 0.49$. (e) Diamond design with varying Possion's ratios ν_0 at the fixed internal surface thickness $t/a = 0.04$. (f) Diamond design with varying internal surface thicknesses t/a at fixed Possion's ratio $\nu_0 = 0.49$.

In general,[80] we can define the direction-dependent effective Young's modulus $E(\hat{\boldsymbol{n}})$,

$$1/E(\hat{\boldsymbol{n}}) = 1/9\kappa + 1/3\mu_2 - (1/\mu_2 - 1/\mu_1)F(\hat{\boldsymbol{n}}), \quad (10)$$

where $F(\hat{\boldsymbol{n}}) = n_1^2 n_2^2 + n_2^2 n_3^2 + n_3^2 n_1^2$, and $\hat{\boldsymbol{n}} = (n_1, n_2, n_3)$ is the unit length directional vector. Similarly, the effective shear modulus G depends on a pair of orthogonal directions represented by unit length vectors $\hat{\boldsymbol{n}}$ and $\hat{\boldsymbol{m}}$,

$$1/G(\hat{\boldsymbol{n}}, \hat{\boldsymbol{m}}) = 1/\mu_1 + (1/\mu_2 - 1/\mu_1)2D(\hat{\boldsymbol{n}}, \hat{\boldsymbol{m}}), \quad (11)$$

where $D(\hat{\boldsymbol{n}}, \hat{\boldsymbol{m}}) = n_1^2 m_1^2 + n_2^2 m_2^2 + n_3^2 m_3^2$. Based on this, taking $\hat{\boldsymbol{n}} = (1, 0, 0)$ and $\hat{\boldsymbol{m}} = (0, 1, 0)$, we recover $G(\hat{\boldsymbol{n}}, \hat{\boldsymbol{m}}) = \mu_1$, which is the shear modulus between two main-axis directions of the cubic unit cell. Taking $\hat{\boldsymbol{n}} = (1, 1, 0)/\sqrt{2}$ and $\hat{\boldsymbol{m}} = (1, -1, 0)/\sqrt{2}$, we obtain $G(\hat{\boldsymbol{n}}, \hat{\boldsymbol{m}}) = \mu_2$, which is the shear modulus between two face-diagonal directions of the cubic unit cell.

Furthermore, we extend our analyses to the Zener ratio,

$$\alpha_r = \frac{\mu_2}{\mu_1} = \frac{2C_{44}}{C_{11} - C_{12}}, \quad (12)$$

which quantifies the extent of anisotropy. As a dimensionless criterion, $\alpha_r = 1$ entails isotropic elasticity. Conversely, the farther away from unity the Zener ratio is, the more anisotropic the metamaterial. In addition, we introduce two additional dimensionless parameters, β_1 and β_2, to quantify the cubic elastic metamaterial's "softness" or "incompressibility,"

$$\beta_1 = \kappa/\mu_1 \quad \text{and} \quad \beta_2 = \kappa/\mu_2. \quad (13)$$

If $\beta_1 \gg 1$ and $\beta_2 \gg 1$, the cubic metamaterial design can be regarded as soft, deformable, compliant, and/or nearly incompressible.

Lastly, we also conduct comprehensive parametric studies on the full ranges of both the base constituent material Poisson's ratio $\nu_0 \in [0, 0.49]$ and internal surface thickness $t/a \in [0.001, 0.1]$.

As shown in Fig. 5a, the effective macroscopic Zener ratio α_r for the primitive unit cell design decreases with increasing internal surface thickness t, though not crossing the limit of $\alpha_r = 1$. Hence, the primitive design remains highly anisotropic in all ranges of internal surface thickness and base constituent material Poisson's ratio. As shown in Fig. 5d, the effective macroscopic $\beta_1 = \kappa/\mu_1$ of the primitive unit cell design decreases when the base constituent material Poisson's ratio ν_0 gets smaller or when the internal surface thickness t gets larger. We also observe a transition from the shear-compliant metamaterial behavior (large β_1) at $\nu_0 = 0.49$ and $t/a = 0.001$ to the compression-compliant metamaterial behavior (small β_1) at $\nu_0 = 0$ and $t/a = 0.01$. By comparison, the effective macroscopic $\beta_2 = \kappa/\mu_2$, plotted in Fig. 5g, is much less sensitive to the internal surface thickness, t, but it is very sensitive to Poisson's ratio ν_0 of the base constituent material.

For the gyroid design, the Zener ratio α_r given in Fig. 5b shows the trend that is opposite to the α_r in Fig. 5a for the primitive design, as it increases monotonically with both Poisson's ratio ν_0 of the base constituent material and the internal surface thickness t. It also stays beyond 1, indicating a robust anisotropic behavior for all ranges of ν_0 and t. As presented in Fig. 5e, the effective macroscopic $\beta_1 = \kappa/\mu_1$ of the gyroid unit cell design monotonically increases together with the base constituent material Poisson's ratio ν_0. The compliance transition is also observed from the shear-compliant metamaterial behavior (large β_1) at $\nu_0 = 0.49$ and $t/a = 0.001$ to the compression-compliant metamaterial behavior (small β_1) at $\nu_0 = 0$ and $t/a = 0.01$, though it is a less sharp transition compared to primitive unit cell design. Meanwhile, as shown in Fig. 5h, the effective macroscopic $\beta_2 = \kappa/\mu_2$ also has a trend of compliance transition that is similar to the case of primitive design when Poisson's ratio ν_0 of the base constituent material increases. We also note that β_2 is relatively less sensitive than β_1 to Poisson's ratio ν_0 of the base constituent material for the gyroid unit cell design.

Figure 5c shows that the effective macroscopic Zener ratio α_r of diamond unit cell design also bears the same trend of monotonic increase with both Poisson's ratio ν_0 of the base constituent material and the internal surface thickness, t. Here, we have a rather special case when the thickness is small $t/a \sim 0.001$: The effective macroscopic Zener ratio α_r reaches $\alpha_r = 1$, as highlighted by the red solid line. This is the only case where isotropic elasticity is possible in the family of all three types of LCP-inspired material designs. Although both the constituent base material property Poisson's ratio and the internal surface thickness contributed to the transition of property from direction-independent to direction-dependent for the diamond unit cell design, the Zener ratio α_r is more sensitive to the internal surface thickness t, and larger t makes the metamaterial more anisotropic. As shown in Fig. 5f, the effective macroscopic $\beta_1 = \kappa/\mu_1$ for the diamond unit cell design also monotonically increases as the constituent base material property Poisson's ratio ν_0 gets higher. Similar to the gyroid unit cell design, the transition of compliance is internal surface thickness independent, i.e., β_1 is not sensitive to the change of t for any constituent base material property Poisson's ratio. Also, we observe the compliance transition from the shear-compliant metamaterial behavior (large β_1) at $\nu_0 = 0.49$ to the compression-compliant metamaterial behavior (small β_1) at $\nu_0 = 0$. In Fig. 5i, especially for a narrow window of internal surface thickness $t/a \in [0.001, 0.03]$, the shear-compliant metamaterial behavior (large β_2) at $t/a = 0.001$ quickly changes to the compression-compliant metamaterial behavior (small β_1) at $t/a = 0.03$. This compliance transition renders the diamond unit cell design the most sensitive case to internal surface thickness t, especially when t is small.

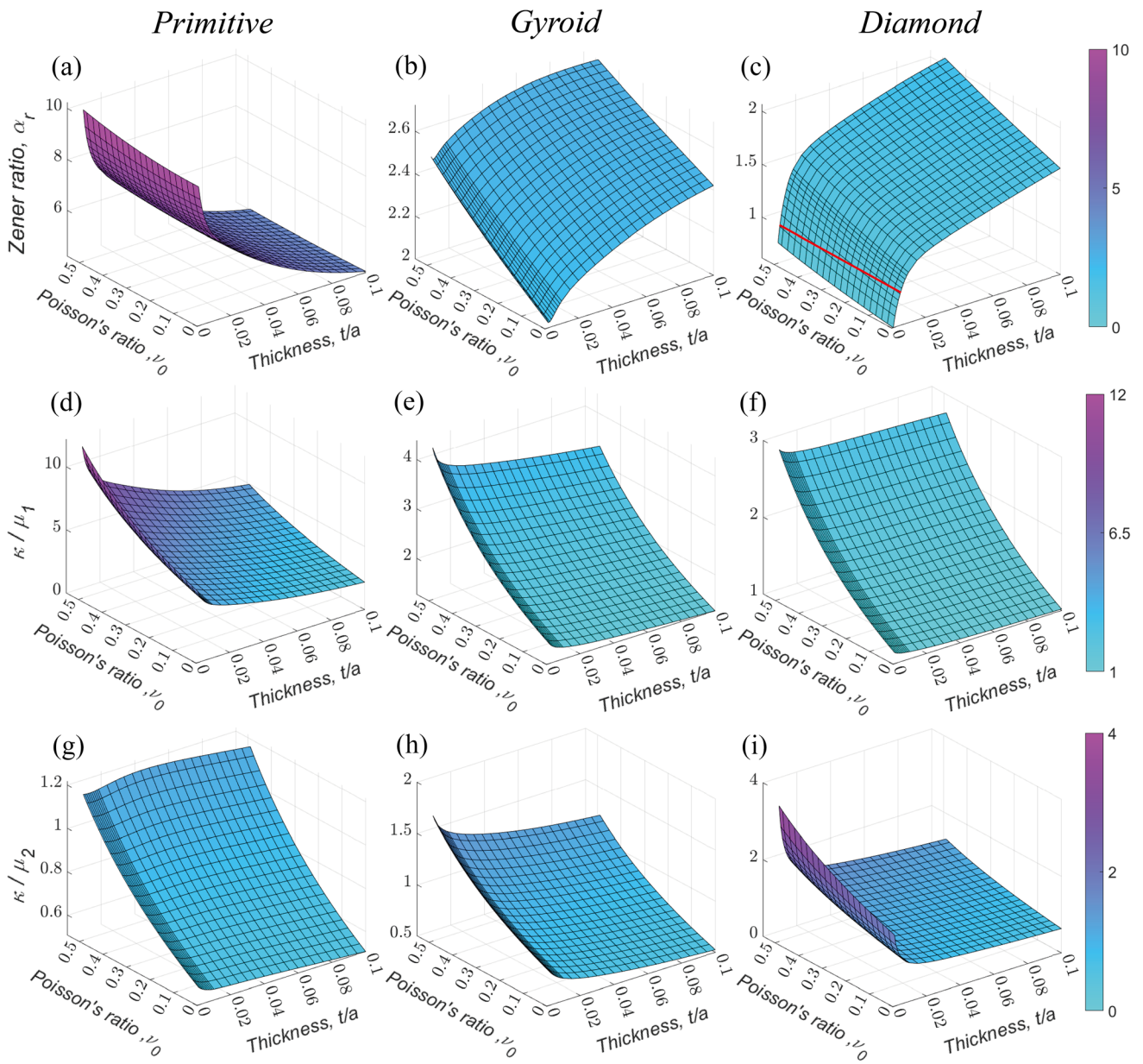

Fig. 5. Comprehensive studies on full ranges of both dimensionless parameters: The internal surface thickness, $t/a \in [0.001, 0.1]$, and Poisson's ratio of base constituent material, $\nu_0 \in [0, 0.49]$. Each row shows a specific effective macroscopic property as a dimensionless measure: (a)–(c) The anisotropy measure Zener ratio, α_r; (d)–(f) the first incompressibility measure, $\beta_1 = \kappa/\mu_1$; (g)–(i) the second incompressibility measure, $\beta_2 = \kappa/\mu_2$. Each column shows a specific unit cell geometry: (a), (d), and (g) for primitive; (b), (e), and (h) for gyroid; (c), (f), and (i) for diamond. The red solid line in (c) indicates the parameter combinations to achieve elastic isotropy, i.e., Zener ratio $\alpha_r = 1$, in the diamond design.

CONCLUSION

In conclusion, we advocate the bio-inspired designs of cubic elastic metamaterials based on the naturally occurring lipidic cubic phase (LCP) morphologies since the surface tension-driven self-assembly process has great potential to become a novel high-throughput fabrication method for many different metamaterials.

Focusing on mechanical properties, we establish a comprehensive framework of geometric construction, finite-element simulation, and post-processing to study the elastic behaviors of three categories of metamaterials mimicking all possible triply periodic minimal surface LCP configurations: primitive type (crystallographic space group $Im\bar{3}m$), gyroid type (space group $Ia\bar{3}d$), and diamond type (space group $Pn\bar{3}m$) unit cells. The effective macroscopic elastic moduli extracted from our rigorous numerical simulations can provide a detailed recipe for metamaterial applications in mechanical and civil engineering settings. The parametric studies on both the internal surface thickness and the base constituent material Poisson's ratio may become good guidance for future manufacturing planning.

Furthermore, we find that, while the primitive design is the most anisotropic, it is possible to achieve isotropic metamaterial by the diamond design with any type of base constituent material. In addition, we observe that all three metamaterial designs behave more like a compression-compliant material with larger internal surface thickness and lower Poisson's ratio of the base constituent material, and they behave more like a shear-compliant material when the internal surface thickness is small and when Poisson's ratio is high in the base constituent material.

We expect that future research efforts will continue to push the frontier of our knowledge further on the LCP-inspired metamaterial in terms of nonlinear elasticity, plasticity, buckling, and fracture, enabling next-generation technological applications in acoustics, photonics, and thermodynamics.

This work was supported by the P.W.'s start-up research funds of the Department of Mechanical Engineering at University of Utah. The support and resources from the Center for High Performance Computing at the University of Utah are gratefully acknowledged. On behalf of all authors, the corresponding author states that there is no conflict of interest.

REFERENCES

1. G. Ma and P. Sheng, *Sci. Adv.* 2, e1501595 (2016).
2. T. Jiang, Q. He, and Z.-K. Peng, *Appl. Phys. Lett.* 112, 261902 (2018).
3. T.A. Schaedler, A.J. Jacobsen, A. Torrents, A.E. Sorensen, J. Lian, J.R. Greer, L. Valdevit, and W.B. Carter, *Science* 334, 962 (2011).
4. A.N. Norris, *Proceed Royal Soc. A: Math. Phys. Eng. Sci.* 464, 2411 (2008).
5. C. Kern, M. Kadic, M. Wegener, *Appl. Phys. Lett.* 107, 132103 (2015).
6. C. Kern, V. Schuster, M. Kadic, and M. Wegener, *Phys. Rev. Appl.* 7, 044001 (2017).
7. T. Bückmann, M. Thiel, M. Kadic, R. Schittny, and M. Wegener, *Nature Commun.* 5, 1 (2014).
8. T. Bückmann, N. Stenger, M. Kadic, J. Kaschke, A. Frölich, T. Kennerknecht, C. Eberl, M. Thiel, and M. Wegener, *Adv. Mater.* 24, 2710 (2012).
9. T. Bückmann, M. Kadic, N. Stenger, M. Thiel, and M. Wegener, On the Feasibility of Pentamode Mechanical Metamaterials, In: The Sixth International Congress on Advanced Electromagnetic Materials in Microwaves and Optics (2012).
10. Y. Xiao, M. Borgh, A. Blinova, T. Ollikainen, J. Ruostekoski, and D. Hall, Topological Superfluid Defects with Discrete Point Group Symmetries, arXiv preprint arXiv: 2203.08186 (2022).
11. J. Park, J.R. Youn, and Y.S. Song, *Phys. Rev. Appl.* 12, 061002 (2019).
12. W. Zhang, Q. Song, W. Zhu, Z. Shen, P. Chong, D.P. Tsai, C. Qiu, and A.Q. Liu, *Adv. Phys.: X* 3, 1417055 (2018).
13. P. Verma, J. Ubaid, K.M. Varadarajan, B.L. Wardle, and S. Kumar, *ACS Appl. Mater. Interfaces.* 14, 8361 (2022).
14. I. Giorgio, M. Spagnuolo, U. Andreaus, D. Scerrato, and A.M. Bersani, *Math. Mech. Solids* 26, 1074 (2021).
15. V.A. Lvov, F.S. Senatov, A.A. Veveris, and V.A. Skrybykina, *Materials* 15, 1439 (2022).
16. C.R. Garcia, J. Correa, D. Espalin, J.H. Barton, R.C. Rumpf, R. Wicker, and V. Gonzalez, *Prog. Electromagnet. Res. Lett.* 34, 75 (2012).
17. S. Kumar, J. Ubaid, R. Abishera, A. Schiffer, and V. Deshpande, *ACS Appl. Mater. Interfaces* 11, 42549 (2019).
18. K. Mohammadi, M.R. Movahhedy, I. Shishkovsky, and R. Hedayati, *Appl. Phys. Lett.* 117, 061901 (2020).
19. J. Baena, L. Jelinek, and R. Marqués *Phys. Rev. B* 76, 245115 (2007).
20. A. Jones, M. Leary, S. Bateman, and M. Easton, *J. Mater. Process. Technol.* 296, 117179 (2021).
21. S. Kazemahvazi, N. Khokar, S. Hallstrom, H. Wadley, and V. Deshpande, *Compos. Sci. Technol.* 127, 95 (2016).
22. L.R. Meza, J.M. Schormans, J.J. Remmers, and V.S. Deshpande, *J. Mech. Phys. Solids* 125, 276 (2019).
23. S. Das, K. Kandan, S. Kazemahvazi, H.N. Wadley, and V.S. Deshpande, *J. Mater. Res.* 33, 317 (2018).
24. P.G. Adams, K.L. Swingle, W.F. Paxton, J.J. Nogan, L.R. Stromberg, M.A. Firestone, H. Mukundan, and G.A. Montaño, *Sci. Rep.* 5, 10331 (2015).
25. R. Parthasarathy and J.T. Groves, *Proc. Natl. Acad. Sci.* 101, 12798 (2004).
26. M. Rappolt, A. Hickel, F. Bringezu, and K. Lohner, *Biophys. J.* 84, 3111 (2003).
27. M. Caffrey, *Acta Crystallogr. Sect. F: Struct. Biol. Commun.* 71, 3 (2015).
28. E.M. Landau, J.P. Rosenbusch, *Proc. Natl. Acad. Sci.* 93, 14532 (1996).
29. A. Chonn, S.C. Semple, and P.R. Cullis, *J. Biol. Chem.* 267, 18759 (1992).
30. M.J. Moghaddam, L. De Campo, L.J. Waddington, A. Weerawardena, N. Kirby, and C.J. Drummond, *Soft Matter* 7, 10994 (2011).
31. J.W. Lee, J.H. Park, and J.R. Robinson, *J. Pharm. Sci.* 89, 850 (2000).
32. H. Yin, X. Huang, F. Scarpa, G. Wen, Y. Chen, and C. Zhang, *Compos. Struct.* 192, 516 (2018).
33. H. Yuk, B. Lu, and X. Zhao, *Chem. Soc. Rev.* 48, 1642 (2019).
34. Y. Li, X. Bai, T. Yang, H. Luo, and C.-W. Qiu, *Nat. Commun.* 9, 273 (2018).
35. G. Rummel, A. Hardmeyer, C. Widmer, M.L. Chiu, P. Nollert, K.P. Locher, I. Pedruzzi, E.M. Landau, and J.P. Rosenbusch, *J. Struct. Biol.* 121, 82 (1998).
36. V. Cherezov, J. Clogston, M.Z. Papiz, and M. Caffrey, *J. Mol. Biol.* 357, 1605 (2006).
37. Y. Kang, X.E. Zhou, X. Gao, Y. He, W. Liu, A. Ishchenko, A. Barty, T.A. White, O. Yefanov, G.W. Han, and Q. Xu, *Nature* 523, 561 (2015).
38. Y. La, C. Park, T.J. Shin, S.H. Joo, S. Kang, and K.T. Kim, *Nat. Chem.* 6, 534 (2014).
39. R. Negrini and R. Mezzenga, *Langmuir* 28, 16455 (2012).
40. A.I. Tyler, H.M. Barriga, E.S. Parsons, N.L. McCarthy, O. Ces, R.V. Law, J.M. Seddon, and N.J. Brooks, *Soft Matter* 11, 3279 (2015).
41. J.M. Seddon, A.M. Squires, C.E. Conn, O. Ces, A.J. Heron, X. Mulet, G.C. Shearman, and R.H. Templer, *Philos. Trans. Royal Soc. A: Math. Phys. Eng. Sci.* 364, 2635 (2006).
42. V. Vitkova and A.G. Petrov, Lipid Bilayers and Membranes: Material Properties, In: *Advances in planar lipid bilayers and liposomes*, Vol. 17 (Elsevier) pp. 89–138 , (2013).
43. J. Briggs and M. Caffrey, *Biophys. J.* 66, 573 (1994).
44. M. Caffrey, *Curr. Opin. Struct. Biol.* 10, 486 (2000).
45. M. Caffrey and V. Cherezov, *Nat. Protoc.* 4, 706 (2009).
46. J. Jouhet, *Front. Plant Sci.* 4, 494 (2013).
47. A. Ridolfi, B. Humphreys, L. Caselli, C. Montis, T. Nylander, D. Berti, M. Brucale, and F. Valle, *Colloids Surf.*, B 210, 112231 (2022).
48. D.L. Gater, V. Réat, G. Czaplicki, O. Saurel, A. Milon, F. Jolibois, and V. Cherezov, *Langmuir* 29, 8031 (2013).
49. O. Al-Ketan, D.-W. Lee, R. Rowshan, and R.K.A. Al-Rub, *J. Mech. Behav. Biomed. Mater.* 102, 103520 (2020).
50. E. Yang, M. Leary, B. Lozanovski, D. Downing, M. Mazur, A. Sarker, A. Khorasani, A. Jones, T. Maconachie, S.

Bateman, and M. Easton, *Mater. Design* 184, 108165 (2019).
51. T. Maconachie, R. Tino, B. Lozanovski, M. Watson, A. Jones, C. Pandelidi, A. Alghamdi, A. Almalki, D. Downing, M. Brandt, and M. Leary, *Int. J. Adv. Manuf. Technol.* 107, 4449 (2020).
52. D. Downing, A. Jones, M. Brandt, and M. Leary, *Mater. Design* 197, 109096 (2021).
53. C. Speziale, R. Ghanbari, and R. Mezzenga, *Langmuir* 34, 5052 (2018).
54. F. Greco, L. Leonetti, A. Pranno, and S. Rudykh, *Compos. Struct.* 233, 111625 (2020).
55. M.M. Alam and K. Aramaki, *J. Colloid Interface Sci.* 336, 329 (2009).
56. M.M. Alam and R. Mezzenga, *Langmuir* 27, 6171 (2011).
57. R. Mezzenga, C. Meyer, C. Servais, A.I. Romoscanu, L. Sagalowicz, and R.C. Hayward, *Langmuir* 21, 3322 (2005).
58. L. Sagalowicz, R. Mezzenga, and M.E. Leser, *Current Opinion in Coll. Interface Sci.* 11, 224 (2006).
59. C. Rodriguez-Abreu, D.P. Acharya, K. Aramaki, and H. Kunieda, *Coll. Surf., A* 269, 59 (2005).
60. C. Rodríguez-Abreu, M. García-Roman, and H. Kunieda, *Langmuir* 20, 5235 (2004).
61. M. Pouzot, R. Mezzenga, M. Leser, L. Sagalowicz, S. Guillot, and O. Glatter, *Langmuir* 23, 9618 (2007).
62. H. Chung, M. Caffrey, *Nature* 368, 224 (1994).
63. S. Jain, X. Gong, L. Scriven, and F.S. Bates, *Phys. Rev. Lett.* 96, 138304 (2006).
64. V. Percec, D.A. Wilson, P. Leowanawat, C.J. Wilson, A.D. Hughes, M.S. Kaucher, D.A. Hammer, D.H. Levine, A.J. Kim, F.S. Bates, and K.P. Davis, *Science* 328, 1009 (2010).
65. I. Maskery, L. Sturm, A.O. Aremu, A. Panesar, C.B. Williams, C.J. Tuck, R.D. Wildman, I.A. Ashcroft, and R.J. Hague, *Polymer* 152, 62 (2018).
66. D.W. Abueidda, R.K.A. Al-Rub, A.S. Dalaq, D.-W. Lee, K.A. Khan, and I. Jasiuk, *Mech. Mater.* 95, 102 (2016).
67. D.W. Abueidda, I. Jasiuk, and N.A. Sobh, *Mater. Design* 145, 20 (2018).
68. D.W. Abueidda, M. Elhebeary, C.-S.A. Shiang, S. Pang, R.K.A. Al-Rub, and I.M. Jasiuk, *Materi. Design* 165, 107597 (2019).
69. D.W. Abueidda, M. Bakir, R.K.A. Al-Rub, J.S. Bergström, and N.A. Sobh, I. Jasiuk, *Mater. Design* 122, 255 (2017).
70. K.A. Khan and R.K.A. Al-Rub, *Int. J. Mech. Sci.* 126, 106 (2017).
71. K.A. Khan and R.K. Abu Al-Rub, *J. Eng. Mech.* 144, 04018029 (2018).
72. K.A. Khan and R.K. Abu Al-Rub, *Mech. Adv. Mater. Struct.* 27, 775 (2020).
73. S. Restrepo, S. Ocampo, J. Ramírez, C. Paucar, and C. García, *J. Phys.: Conf. Series* 935, 012036 (2017).
74. L. Zhang, S. Feih, S. Daynes, S. Chang, and M.Y. Wang, J. Wei, W.F. Lu, *Addit. Manuf.* 23, 505 (2018).
75. O. Al-Ketan, R. Rowshan, and R.K.A. Al-Rub, *Addit. Manuf.* 19, 167 (2018).
76. M. Afshar, A.P. Anaraki, H. Montazerian, and J. Kadkhodapour, *J. Mech. Behav. Biomed. Mater.* 62, 481 (2016).
77. S.M. Giannitelli, D. Accoto, M. Trombetta, and A. Rainer, *Acta Biomater.* 10, 580 (2014).
78. A. Jones, M. Leary, S. Bateman, and M. Easton, *Softw. Impacts* 10, 100167 (2021).
79. O. Al-Ketan and R.K. Abu Al-Rub, Mslattice, *Mater. Design Process. Commun.* 3, e205 (2021).
80. A.N. Norris, *Proceed. Royal Soc. A: Math. Phys. Eng. Sci.* 462, 3385 (2006).
81. M.A. Hayes, A.N. Norris, and Q., *J. Mech. Appl. Math.* 45, 141 (1992).
82. A.N. Norris and Q., *J. Mech. Appl. Math.* 42, 413 (1989).
83. P. Paufler, *Acta Crystallogr. Sect. A: Found. Crystallograp.* 62, 316 (2006).
84. S. Timoshenko and J.N. Goodier, Theory of Elasticity: by S. Timoshenko and JN Goodier (McGraw-Hill), (1951).
85. T. Thomas, *Proc. Natl. Acad. Sci.* 55, 235 (1966).
86. J.F. Nye et al., *Physical Properties of Crystals: Their Representation by Tensors and Matrices* (Oxford University Press), (1985).
87. L. Landau and E. Lifshitz, *Theory of Elasticity*. Butterworth-heinemann (1986).
88. T. Ting, *Math. Mech. Solids* 1, 301 (1996).
89. D. Royer and E. Dieulesaint, *Elastic Waves in Solids I: Free and Guided Propagation* (Springer Science & Business Media), (1999).
90. J.R. Barber, Elasticity Springer, (2002).
91. J.J.M. Carcione, *Wave Fields in Real Media: Wave Propagation in Anisotropic, Anelastic, Porous and Electromagnetic Media* (Elsevier, 2007).
92. M.H. Sadd, *Elasticity: Theory, Applications, and Numerics* (Academic Press, 2009).
93. A.I. Lurie, *Theory of Elasticity* (Springer Science & Business Media), (2010).
94. R. Brannon, Rotation, Reflection, Frame Changes, In: *Orthogonal Tensors in Computational Engineering Mechanics* (IOP Publishing), (2018).
95. H. Le Quang, Q.-C. He, and N. Auffray, *Proceed. Royal Soc. A* 477, 20210165 (2021).
96. J.N. Reddy, *An Introduction to Continuum Mechanics* (Cambridge University Press), (2013).
97. P. Chadwick, M. Vianello, and S.C. Cowin, *J. Mech. Phys. Solids* 49, 2471 (2001).
98. S.C. Cowin, *Continuum Mechanics of Anisotropic Materials* (Springer Science & Business Media, 2013).
99. P. Zhang and P. Wang, *Front. Mech. Eng.* 7, 704192 (2021).
100. G.M. Yunya L., Christian K., and P.W., *A Soc. Eng. Sci.* (2022).
101. P. Wang, J. Shim, and K. Bertoldi, *Phys. Rev. B* 88, 014304 (2013).
102. Q. Ma, L. Zhang, J. Ding, S. Qu, J. Fu, M. Zhou, M.W. Fu, X. Song, and M.Y. Wang, *Addit. Manuf.* 47, 102293 (2021).
103. D. Regan, J. Williams, P. Borri, and W. Langbein, *Langmuir* 35, 13805 (2019).
104. T. Jadidi, H. Seyyed-Allaei, M.R.R. Tabar, and A. Mashaghi, *Front. Bioeng. Biotechnol.* 2, 8 (2014).